Intrinsic conductance of domain walls in $BiFeO_3$

Yi Zhang[1†], Haidong Lu[2†], Xingxu Yan[1†], Xiaoxing Cheng[3], Toshihiro Aoki[5], Linze Li[1], Colin Heikes[6], Daniel S. P. Lau[8], Darrell G. Schlom[6,7], Longqing Chen[3], Alexei Gruverman[2*], and Xiaoqing Pan[1,4,5*]

[1]*Department of Materials Science and Engineering University of California – Irvine, CA 92697, USA*

[2]*Department of Physics and Astronomy & Nebraska Center for Materials and Nanoscience, University of Nebraska, Lincoln, NE 68588, USA*

[3]*Department of Materials Science and Engineering, Penn State University, University Park, Pennsylvania 16802, USA*

[4]*Department of Physics and Astronomy University of California – Irvine, CA 92697, USA*

[5]*Irvine Materials Research Institute, University of California, Irvine, CA 92697, USA.*

[6]*Department of Materials Science and Engineering, Cornell University, Ithaca, New York 14853, USA*

[7]*Kavli Institute at Cornell for Nanoscale Science, Ithaca, New York 14853, USA*

[8]*Department of Applied Physics, The Hong Kong Polytechnic University, Hung Hom, Kowloon, Hong Kong*

[†] These authors contributed equally to this work.

*To whom correspondence and requests for materials should be addressed. E-mail: xiaoqing.pan@uci.edu (X.Q.P.) and agruverman2@unl.edu (A.G.)

Ferroelectric domain walls are two-dimensional (2D) structural boundaries that separate regions with different orientations of electrical polarization-domains[1], which exhibit functional characteristics that are completely different from the domains that they delineate. For example, it has been shown that they may be metallic[2] or even

superconducting[3], while the domains that they separate are insulating. Recent research shows that the domain walls can exhibit their own distinct chemistry and magnetic behavior[4-9]. These emergent characteristics have fostered the realization that the domain walls can be used as functional elements in novel nanoelectronic devices[10-13]. Here, we report observation of the intrinsic conductivity of the 71° and 109° domain walls by probing the local conductance over a cross-section of the $BiFeO_3/TbScO_3$ (001) thin film heterostructures. Through a combination of conductive atomic force microscopy, high-resolution electron energy loss spectroscopy and phase-field simulations, we show that the 71° domain walls exhibit conductivity, which is about an order of magnitude larger than that of the 109° domain walls. More importantly, we demonstrate high anisotropy of the 71° domain walls conductivity: while they are conducting along the $[010]_p$ direction, they show much lower conductivity along the $[001]_p$ direction. High resolutions electron energy loss spectroscopy (EELS) reveals a band gap lowering at the 71° domain walls and only a little change at the 109° domain walls. The phase-field simulations reveal a charged nature of the 71° walls compared to almost neutral 109° walls, suggesting that charge-induced band gap lowering is the main mechanism behind the intrinsic conductivity of the 71° domain walls. Furthermore, it is found that the conductivity of the 71° walls alternates between the adjacent walls due to a potential distribution variation. The origin of the anisotropic conductivity of the 71° walls stems from the potential discontinuity of the 71° domain walls along the $[110]_p$ direction. It is emphasized that the domain wall conductivity measured in the direction normal to the film surface - exprimental geometry used in most of the previous works - does not reveal the true conductivity of the 71° domain walls.

A single-phase multiferroic $BiFeO_3$ (BFO) is the material where the intriguing electrical conductivity of the domain walls has been first reported[14-16]. Since then, numerous studies have been performed to investigate the conducting properties of the 71° and 109° walls. The experimental results generally indicate that the 71° domain walls are more insulating as compared with the 109° walls[17-19]. Lubk et al.[20] suggested that the domain wall conductivity in BFO originated from the lowering of the band gap at the walls, with the band gap change at the 109° walls being larger than at the 71°

walls. Several other mechanisms have been proposed, such as flexoelectric effect, octahedral rotation, oxygen vacancy migrating, chemical doping, domain wall geometry and charge defect, etc[21-26]. However, two main issues remain to be addressed. First, most of the BFO materials in these studies are either defect-rich or element dopped, which makes it difficult to separate the intrinsic conductivity of the domain walls from the effects of extrinsic factors[17,22, 26, 27]. Second, in the previous studies, the domain wall conductivity is usually measured in the direction perpendicular to the film surface, i.e. by applying an electrical bias between the bottom electrode and the probing tip in contact with the domain wall[9,17]. In this geometry, the results may be affected by domain wall discontinunity, inhomogeneous defect and charge distributions at the domain walls, or domain wall bending and curving[28,29]. Because of these factors, there was a strong variation in the transport properties of BFO domain walls reported in the previous works[17,21, 27, 30-33]. Hence, for better understanding of the origin of the intrinsic domain wall conductivity, the deployment of experimental geometry and samples with carefully controlled electrical boundary conditions and domain structure is highly desirable.

In this work, the electrical transport properties of the as-grown 71° and 109° domain walls in the $BiFeO_3/TbScO_3$ (001) thin film heterostructures have been studied by means of conductive atomic force microscopy (CAFM) along two directions, i.e., parallel to and perpendicular to the film surface. We employ a multimodal testing approach based on a combination of piezoresponse force microscopy (PFM) and aberration-corrected transmission electron microscopy (TEM) characterization of the same specimens. This approach allows cross-correlation analysis of the TEM, PFM, and CAFM data enabling direct comparison of the domain wall conductivity with the local polarization configuration, structural defects and local chemistry at the atomic scale.

The 200-nm- and 400-nm-thick $(001)_p$ oriented $BiFeO_3$ (BFO) thin films with ordered 71° and 109° domain structures grown by molecular-beam epitaxial (MBE) on insulating $(110)_o$ $TbScO_3$ (TSO) single-crystalline substrates have been used in this study (*p* and *o* subscripts represent pseudocubic and orthorhombic indices,

respectively). Details of film growth are given in Methods. To test the domain wall conductivity, we carried out PFM and CAFM mapping on the cross-sections of the BFO/TSO heterostructures cut perpendicular to the 71° or 109° domain stripes (Figures 1a and 1f). Details of the specimen preparation and the schematic of the geometry of the CAFM measurements are shown in Ref. [34]. In Figure 1b, the vertical-PFM image acquired on the sample cross-section shows typical 71° periodical domain arrays, which is consistent with the bright-field TEM image (see Supplementary Figure 1). Upon close examination, a slight curvature of the walls at the top interface vicinity can be seen. Figure 1c shows a CAFM image of the same region as in Figure 1b, which was acquired under an applied dc bias of 2 V. The CAFM contrast shows a strong current signal stemming from the 71° domain walls, indicating that these walls are conductive along the $[010]_p$ direction (which is parallel to the film surface). Interestingly, an alternating levels of conductivity can be observed at the adjacent 71° walls (marked as DW1 and DW2 in Figures 1b and 1c), which is also clearly illustrated by the current profile line in Figure 1d. The *I-V* curves in Figure 1e further confirm this difference in conductivity between the adjacent 71° domain walls.

Conductivity of 109° walls along the $[010]_p$ direction was examined exactly in the same way (Figure 1f). The vertical PFM image of the 109° domain structure on the sample cross-section (Figure 1g) is consistent with the TEM data shown in Supplementary Figure 2. In contrast to the 71° domain walls, CAFM mapping of the 109° walls did not reveal any current above the noise level (Figure 1h). (Note the conducting behavior of the BFO/TSO interface induced by the ferroelectric polarization of BFO has been discussed elsewhere [34]). The low-conducting nature of the 109° walls along the $[010]_p$ direction is illustrated by the current profile and the *I-V* spectroscopic measurements (Figures 1i and 1j). In addition, a difference in conductivity between the 71° and 109° walls along the $[010]_p$ direction has been further demonstrated by testing the mixed domain regions in another sample (see Supplementary Figure 3). Detailed analysis shows that the conductivity of the 71° domain walls is at least an order of magnitude larger than that of the 109° domain walls.

The band gap of domain walls is considered as a critical parameter determining their intrinsic conductivity[20]. However, in the case of BFO, it has not been measured experimentally yet. To fully address the origin of the intrinsic conductivity of domain walls, the band gaps of the 71° and 109° domain walls were analyzed by using atomic-resolution EELS (see Methods for details). High-resolution low-loss EELS line-scans were taken across the 71° and 109° domain walls, respectively (Figures 2a and 2d). The acquired results were averaged within the area along the domain walls. Band gaps around two adjacent 71º domain walls (i.e. DW1 and DW2) and the 109° walls were calculated from the low-loss EELS results, as shown in Figures 2b and 2e. Details of the calculation of band gap energy from the low-loss EELS can be found in Methods. We can see an obvious band gap lowering at the 71° domain walls compared to the bulk BFO, while little change is observed at the 109° domain walls. The lower band gap of the 71° domain walls should lead to higher conductivity in agreement with our CAFM results. Consequently, the core-loss EELS was conducted across the walls and the energy onset difference between O-K and Fe-L_3 edges was extracted to elucidate the chemical shift of local Fe, since there is a linear relationship between this onset energy and the oxidation state of Fe[26,35]. It is found that the energy onset difference of Fe-O at the 71° domain walls is lower than in bulk BFO, indicating a reduced valence state of Fe (see Figure 2c). On the other hand, the energy onset difference of Fe-O at the 109° domain walls keeps intact with respect to the bulk phase (Figure 2f). Therefore, in contrast to the 109° walls, Fe at 71° domain walls has a reduced valence state donating electrons that will compensate the possible bound charges at domain walls.

It has been proposed that the oxygen vacancies play an important role in the conductivity of domain walls[29,36]. To check if this mechanism is also applicable to our BFO films, electron energy-loss spectroscopy (EELS) was used to examine oxygen vacancies at the BFO domain walls. EELS spectra in the Supplementary Figure 4 show no obvious evidence of oxygen vacancies around both 71° and 109° domain walls. Therefore, it can be concluded that oxygen vacancies are not the source of the domain wall conductivity observed in our experiments.

To further examine the domain walls conductivity, CAFM measurements

have been carried out on the film top surface of the BFO/TSO heterostructure. As has been shown recently, a conductive BFO/TSO interface can be used as a bottom electrode[34]. A typical pattern of the ordered 71° stripe domains has been revealed by lateral PFM (Figure 3a). We carried out CAFM mapping (Figure 3b) of the same region under an applied dc bias of +2/-2V and no current signal could be detected at the 71° domain walls. A quantitatively different behavior was observed in the BFO/TSO samples with the 109° domains. Figure 3c shows the vertical PFM image of the BFO top surface, revealing a typical 109° striped domain structure. CAFM image in Figure 3d shows strong current contrast due to the conducting 109° domain walls in agreement with the previously reported results[17,26,27]. The conductivity difference between the 71° and 109° domain walls measured from the film top surface was further confirmed by *I-V* curves (see Supplementary Figure 5).

CAFM results from the cross-section samples confirm that 71° domain walls are generally more conducting than 109° domain walls. However, CAFM data collected in conventional geometry from the film top surface show that 109° domain walls are conducting, while 71° domain walls are insulating. Thus, it appears that both 71° and 109° domain walls show anisotropic conductance. However, in the case of 109º domain walls, the obtained results can be explained simply by the different thicknesses of the tested samples: conductivity is observed in the conventional geometry when the the tip-electrode distance is 400 nm (Figure 3d) while no current was detected in the cross-sectional geometry when the tip-electrode distance was more than 1 μm (Figure 1g). For the 71° walls, the situation is opposite: the conductivity measured on the cross-sectional surface (Figure 1c) is much larger than that detected on the film top surface (Figure 3b). Thus, it can be concluded that in the case of the 71° walls, we indeed observe genuine anisotropic conductance and not the thickness-induced effect.

To clarify a mechanism of the unusual conducting behavior of the 71° walls, phase-field modeling of the charge distribution in the ordered 71° and 109° domain arrays has been carried out[11] (see Methods for details). The simulated domain structures of the 71° and 109° domains are shown in Figures 4a and 4d. For the 71º domains

simulations, we initially assume that the domain walls are planar and the width of the adjacent domains, ***a*** and ***b***, is the same (Figure 4a). In the following, we mark the neighboring 71° domain walls as domain wall 1 (DW1) and domain wall 2 (DW2). For the uniform domain width of 150 nm, i.e. ***a***/***b*** is 150/150, the simulation results show that the bound charge accumulates both at the DW1 and DW2, clearly distinguishing them from the interior of the domain region (Figure 4b). In contrast, in the 109° domain structure (Figure 4d), the charge distributes across the domain interior without accumulation at the domain walls (Figure 4e). Therefore, even in the absence of any structural defects, a typical 71° domain wall is inherently charged, while a 109° domain wall is more close to being neutral. The corresponding potential distributions at the 71° and 109° domain walls induced by the bound charge are shown in Figures 4c and 4f, respectively. It can be seen that the 71° walls exhibit a high potential, while the potential is close to zero at the 109° walls. Just like a charged domain wall, the 71° domain wall contains a higher density of bound charges than the 109° wall, which naturally should be compensated by more free carriers[36]. The remarkable difference in bound charge accumulation and electric potential distribution between the 71° and 109° domain walls explains their drastically different intrinsic conductivity. It should be also noted, that the potential distribution is discontinuous along the 71° domain walls (i.e. $[110]_p$) in the direction from the film/substrate interface to the film surface.

To clarify the origin of the conductance difference between the adjacent 71° domain walls, the previous phase-field model was expanded by considering the effect of uneven width of the adjacent domains (Figure 4a). When the ***a***/***b*** ratio gradually changes from 150/150 to 100/200, the potential of the DW1 turns more positive, while DW2 becomes partially negative (Figure 4g-i). The potential profiles along the domain walls in the $[110]_p$ direction changing with the ***a***/***b*** ratio are shown in Supplementary Figure 6. Naturally, the strong positive potential leads to electron accumulation and results in high conductivity of the DW1. In contrast, a low positive potential attracts fewer electrons and leads to lower conductivity in the DW2. The charge density related conductivity difference between the adjacent 71° domain walls is in agreement with the EELS and CAFM results in Figure 2 and Figure 1.

In our experiments, the averaged ***a***/***b*** ratio was estimated to be in the range between 130/170 and 110/190. For this kind of domain configuration, we note that the potential distribution is generally not continuous along the $[110]_p$ direction according to the simulation results. As schematically shown in Figure 4j, this discontinuity of potential distribution may induce a potential barrier along the wall forming a p-n junction, which will obstruct the conducting path along the 71° domain walls in the film thickness direction (i.e. $[110]_p$) when measurement is taken on the film top surface. Moreover, the domain wall curvature can also induce a local potential change and strengthen the potential discontinuity along the 71° domain walls[29] (see Supplementary Figure 7), which could serve as another source of the anisotropic conductance of the 71° domain walls.

Thus, according to the phase-field simulation results, the conducting channel along the 71° domain walls in the film thickness direction is likely perturbed by the potential discontinuity, which explains the absence of the CAFM signal in Figure 3b. Therefore, their anisotropic conductance does not contradict the general conductive nature of the 71° domain walls. The potential discontunity induced by the 71º domain wall curvature may be another reason behind the controversy regarding the conflicting reports on the conductance of the 71° domain walls[17-19,28,29].

In conclusion, using a combination of the local probe techniques we have revealed the intrinsic conductivity of the 71° and 109° domain walls in BFO thin films. We have found that the intrinsic conductivity of the 71° domain walls is an order of magnitude larger than that of the 109° domain walls. Atomic resolution EELS analysis and phase-field simulation demonstrate a clear band gap lowering and a weakly-charged nature of the 71° domain walls, while a little band gap change is observed at the 109° walls. Furthermore, the electrostatic interaction [37] of the neighboring 71° domain walls and the domain wall curvature can induce an inhomogenous potential distribution along the $[110]_p$ direction, which induces strongly anisotropic conductance of the 71° walls: the insulating or poor conducting behavior along the $[110]_p$ direction and high conductivity in the $[010]_p$ direction. These results deepen our knowledge on the intrinsic conductivity of the BFO domain walls and may help explain the previous

discrepancies regarding the reported variations in domain wall conductivity as well as the role of domain walls in the photovoltaic effect [16,17,19,38]. Due to their anisotropic conductivity, the 71° and 109° domain walls can be used as a new type of local reconfigurable doping elements in the BFO matrix [27,39,40]. This finding, while providing new insights into the fundamental physics of ferroelectric domain walls, may open a possibility for realization of domain wall-based devices with substantially enhanced functionality.

Methods

Sample preparation

The $BiFeO_3$ films were grown on single-crystalline $(110)_o$ $TbScO_3$ substrates by reactive-molecular beam epitaxy (MBE). The 200-nm- and 400-nm-thick $BiFeO_3$ film were deposited at 650 °C in distilled ozone (~80% ozone) at pp 4×10^{-6} Torr. Cross-sectional TEM samples were prepared by conventional mechanical polishing followed by argon ion milling. The specimens preparation for CAFM is the same with that of regular TEM. The thickness of the specimens for CAFM is several micrometers. See details in the Supplementary Materials.

Structural and Electrical characterization

High-resolution STEM-EELS experiments were performed at UC, Irvine, by Nion UltraSTEM 200 equipped with C3/C5 corrector and high-energy resolution monochromated EELS system (HERMES). The instrument was operated at 100 kV with convergence semi-angle of 30mrad and with a beam current of ~100 pA. For analyzing band gap information, low-loss EELS mapping is acquired with a dispersion of 0.05 V/channel and dwell time of 10 ms/pixel. By modulating monochromator, the energy resolution reaches about 0.1 eV, which are capable to obtain the bandgap change at about 2.6 eV and provide sufficient intensity for fitting curve. Because $BiFeO_3$ has been confirmed to possess direct band gap, the band gap energy is extracted by fitting the curve of direct band gap with the following equation[41,42],

$I=c(E-E_g)^{0.5}$

where I is spectrum intensity, c is coefficient, E is energy loss and E_g is direct band gap energy. For investigation of Fe oxidation state, a dispersion of 0.28eV/channel was used to acquire both O-K and Fe-L_3 edges in same spectrum and the dwell time was 0.4 s/pixel. The background in each spectrum was removed by power-law function in commercial software package DigitalMicrograph. The energy loss where the edge reaches 10% of its maximum intensity is taken as the energy onset value for each O-K and Fe-L_3 edge in each pixel.

PFM measurements were performed using a commercial Asylum Research MFP-3D system. Nanosensors PPP–EFM cantilever was used in this study. 3D vector PFM imaging was performed by collecting a vertical piezoresponse component and two lateral piezoresponse components. The sample was rotated by 90° to discriminate between orthogonally oriented in-plane polar vector components.

The CAFM measurements were carried out using the same MFP-3D system. Conductive diamond-coated probes with a nominal force constant of 16N/m were used for all CAFM measurements. The details of the BFO/TSO cross-sectional specimens preparation for measurements can be seen in Supplementary Materials. The CAFM images were acquired with a dc bias of 2V applied to the bottom electrode.

Phase-field simulation

Phase-field simulation provides information of polarization evolution by solving the time-dependent Ginzburg-Landau equation:

$$\frac{\partial P_i(\mathbf{r},t)}{\partial t} = -L\frac{\delta F}{\delta P_i(\mathbf{r},t)}, (i = 1,2,3)$$

where P_i is the order parameter in Landau theory, and its physical meaning is the component of polarization in the i-th direction. L is the kinetic coefficient, r represents the spatial position vector, t denotes the evolution time step, and F is the total free energy which can be expressed by the following fomular.

$$F = \int (f_{landau} + f_{elastic} + f_{electric} + f_{gradient})dV$$

Detailed expressions of the energy density as well as the method of solving the phase-field equations can be found in literature[43-46]. All the parameters are taken from literature[46,47].

Due to the large size of the experiment domain, which is beyond the computation resources we have access to, and on the other hand, since our focus is on the film substrate interface, we are able to scaled down the system size while not compensating the physical phenomena at the interface.

The size of the simulation system is 200*100*45 grids, with each grid point representing 1nm in real space. The thickness of the substrate, film and air layer is 10 nm, 30 nm and 5 nm respectively. For the x and y directions, a periodic boundary condition is adopted. Initial setup for the simulation is a series of 109° domain strips, each 30 nm in width, along the y direciton. The elastic boundary condition is fix displacement 10 grid into the substrate and traction free on top of film surface. And it is assumed no mismatch strain between film and substrate. The electric boundary condition is short circuit for both film top surface and bottom interface, as in experiment the *I-V* curve measurement suggest even though there is no electrode, there are still free charges available to compensate the polarization bound charges. In phase-field simulation, the bound charge distribution is obtained by calculating derivatives of polarizations, and the electric potential distribution is then computed by solving the Poisson's equation.

References

1. Gregg, J. M. and Kumar, A. Applied physics: Trawling for complements, *Nature* **510**, 481 (2014).
2. Sluka,T., Tagantsev,A. K., Bednyakov P. and Setter, N. Free-electron gas at charged domain walls in insulating $BaTiO_3$, *Nat. Comms.* **4**, 1808 (2013).
3. Aird, A. and Salje, H. Sheet superconductivity in twin walls: experimental evidence of WO_{3-x}, *J. Phys.: Condens. Matter* **10**, L377 (1998).
4. Farokhipoor, S. et al. Artificial chemical and magnetic structure at the domain walls of an epitaxial oxide, *Nature* **515**, 379 (2014).
5. Seidel, J. et al. Domain wall functionality in $BiFeO_3$, *Phase Transitions* **86**, 53(2013).
6. Campbell, M. P. et al. Hall effect in charged conducting ferroelectric domain walls,

Nature Communications **7**, 13764 (2016)
7. Gareeva, Z. et al. Complex domain walls in $BiFeO_3$, *Physical Review B* **91**, 060404(R) (2015).
8. Sluka, T. et al. Free-electron gas at charged domain walls in insulating $BaTiO_3$, *Nature Communications* **4**,1808 (2013).
9. Guyonnet, J. et al. Conduction at Domain Walls in Insulating $Pb(Zr_{0.2}Ti_{0.8})O_3$ Thin Films, *Advanced Materials* **23**, 5377 (2011)
10. Catalan, G. et al. Domain wall nanoelectronics, *Review of modern physics* **84**,119 (2012).
11. Li, L. Z. et al. Giant Resistive Switching via Control of Ferroelectric Charged Domain Walls, *Advanced Materials* **28**, 6574 (2016)
12. Ju, C. C. et al. Anomalous Electronic Anisotropy Triggered by Ferroelastic Coupling in Multiferroic Heterostructures, *Advanced Materials* **28**, 876-883 (2016).
13. Seidel, J. et al. Electronic Properties of Isosymmetric Phase Boundaries in Highly Strained Ca-Doped $BiFeO_3$, *Advanced Materials* **26**, 4189 (2014).
14. Yang, J. C. et al. $BiFeO_3$ Thin Films:A Playground for Exploring Electric-Field Control of Multifunctionalities, *Annu. Rev. Mater. Res.* **45**:249-75 (2015).
15. Seidel, J. et al. Topological Structures in Multiferroics-Domain Walls, Skyrmions and Vortices, *Advanced Electronic Materials* **2**, 1500292 (2016)
16. Yang, S. Y. et al. Above-bandgap voltages from ferroelectric photovoltaic devices, *Nature Nanotechnology* **5**,143 (2010).
17. Seidel, J. et al. Conduction at domain walls in oxide multiferroics, *Nature Mateirals* **8**, 229 (2009).
18. Jang, H. W. et al. Domain Engineering for Enhanced Ferroelectric Properties of Epitaxial (001) $BiFeO_3$ Thin Films, *Advanced Materials* **21**, 817-823 (2009).
19. Chiu, Y. P. et al. Atomic-Scale Evolution of Local Electronic Structure Across Multiferroic Domain Walls, *Advanced Materials* **23**, 1530-1534 (2011).
20. Lubk, A. et al. First-principles study of ferroelectric domain walls in multiferroic bismuth ferrite, Physical Review B, 80, 104110 (2009).
21. Farokhipoor, S. et al. Conduction through 71° Domain Walls in $BiFeO_3$ Thin Films, *Physical Review Letters* **107**, 127601 (2011).
22. Maksymovych, P. et al. Dynamic Conductivity of Ferroelectric Domain Walls in $BiFeO_3$, *Nano Letters* **11**, 1906-1912 (2011)
23. Catalan, G. On the Link Beween Octahedral Rotations and Conductivity in the Domain Walls of $BiFeO_3$, *Ferroelectric* **433**, 65 (2012).
24. Seidel, J. et al. Domain Wall Conductivity in La-Doped $BiFeO_3$, *Physical Review Letters* **105**, 197603 (2010).
25. Vasudevan, R. K. et al. Domain Wall Geometry Controls Conduction in Ferroelectrics, *Nano Letters* **12**, 5524-5531(2012).
26. Rojac, T. et al.Domain-wall conduction in ferroelectric $BiFeO_3$ controlled by accumulation of charged defects, *Nature Mateirals* **10**, 4799 (2016).
27. Crassous, A. et al. Polarization charge as a reconfigurable quasi-dopant in ferroelectric thin films, *Nature Nanothechology* **10**, 614 (2015).
28. Choudhury, N. et al. Geometric frustration in compositionally modulated

ferroelectrics, *Nature* **470**, 513 (2011).
29. Tselev, A. et al. Microwave a.c. conductivity of domain walls in ferroelectric thin films, *Nature Commnunications* **7**, 11630 (2016).
30. Prosandeev, S. et al. Displacement Current in Domain Walls of Bismuth Ferrite, *npj Computating Materials* **4**, 8 (2018).
31. Vasudevan, R. K. et al. Field enhancement of electronic conductance at ferroelectric domain walls, *Nature Communications* **8**,1318 (2017).
32. Sharma, P. et al. Nonvolatile ferroelectric domain wall memory, *Science Advances* **3**, 6 (2017).
33. Jiang, J. et al. Temporary formation of highly conducting domain walls for non-destructive read-out of ferroelectric domain-wall resistance switching memories, *Nature Materials* **17**, 49-56 (2018).
34. Zhang, Y. et al. Direct observation of strongly anisotropic polarization-induced conduction at the ferroelectric/insulator interface, *Nature Nanotechnology* **13**, 1132 (2018).
35. Tan, H. Y., Verbeeck, J., Abakumov, A., Tendeloo, G. V. Oxidation state and chemical shift investigation in transition metal oxides by EELS, *Ultramicroscopy* **24**, 116 (2012).
36. Sluka, T. et al. Enhanced electromechanical response of ferroelectrics due to charged domain walls, *Nature Commnunications* **3**, 748 (2012).
37. Ievlev, A. V. et al. Intermittency, quasiperiodicity and chaos in probe-induced ferroelectric domain switching, *Nature Physics* **10**, 59 (2014).
38. Matsuo, H. et al. Bulk and domain-wall effects in ferroelectric photovoltaics, *Physical Review B* **94**, 214111 (2016).
39. Eliseev, E. A., Morozovska, A. N., Svechnikov, G. S., Maksymovych, P. & Kalinin, S. V. Domain wall conduction in multiaxial ferroelectrics. *Phys. Rev. B* **85**, 045312 (2012).
40. Maksymovych, P. Complex oxide ferroelectrics: Electrostatic doping by domain walls, *Nature Nanotechnology* **10**, 517 (2015).
41. Rafferty, B. and Brown, L. M., Direct and indirect transitions in the region of the band gap using electron-energy-loss spectroscopy, *Physical Review B* **58**, 10326 (1998).
42. Gu L. et al., Band-gap measurements of direct and indirect semiconductors usingmonochromated electrons, *Physical Review B* **75**, 195214 (2007).
43. Li, Y. et al. Effects of the substrate constraint on the stability and evolution of ferroelectric domain structures in thin films, *Acta Mater.* **50**, 395-411(2002).
44. Li, Y. L. et al. Effect of electrical boundary conductions on ferroelectric domain structures in thin films, *Appl. Phys. Lett.* **81**, 427 (2002).
45. Chen, L. et al. Application of semi-implicit Fouriter-spectral method to phase field equations, *Comput. Phys. Commun.* **108**, 147-158 (1998).
46. Xue, F. et al. Orientations of low-energy domain walls in perovskites with oxygen octahedral tilts, *Phys. Rev. B* **, 90**, 220101 (2014).
47. Li, Q. et al. Giant elastic tunability in strained BiFeO3 near an electrically induced phase trasition, Nat. Commun. **6**, 8985 (2015).

Acknowledgements

The work was supported by the Department of Energy (DOE) under Grant DE-SC0014430(Y. Zhang, X. X. Yan, L. Z. Li, and X. Q. Pan). The research at the University of Nebraska-Lincoln was supported by the National Science Foundation through the Nebraska Materials Science and Engineering Center (MRSEC, Grant No. DMR-1420645) and by Grant No. DMR-1709237(H.L., and A.G.). The work at Penn State is supported by the U.S. Department of Energy, Office of Basic Energy Sciences, Division of Materials Sciences and Engineering under Award DE-FG02-07ER46417.The work at Cornell University was supported by the National Science Foundation (Nanosystems Engineering Research Center for Translational Applications of Nanoscale Multiferroic Systems) under grant number EEC-1160504 (C.H. and D.G.S.). Substrate preparation was performed in part at the Cornell Nanoscale Facility, a member of the National Nanotechnology Coordinated Infrastructure (NNCI), which is supported by the National Science Foundation (Grant ECCS-1542081).

Author contributions

X.Q.P and Y.Z. conceived this project and designed experiments. Y.Z. and H.L. carried out the scanning probe microscopy experiments and data analysis supervised by A.G. and X.Q.P. X.X.Y. and Y. Z. carried out the transmission electron microscopy and EELS studies supervised by X.Q.P. X.X.C carried out the phase field simulations supervised by L.Q.C. The EELS characterization was assisted by T.A. L. L. and S.P.L. participated in the analysis of experimental data. Thin films were grown by C.H. supervised by D.G.S. Y.Z., H.L., A.G. and X.P. wrote the manuscript with help from all the other authors.

Additional information

Supplementary information is available in the online version of the paper. Reprints and permissions information is available online at www.nature.com/reprints. Correspondence and requests for materials should be addressed to

A.G.(agruverman2@unl.edu) and X.Q.P. (xiaoqing.pan@uci.edu).

Competing financial interests

The authors declare no competing financial interests.

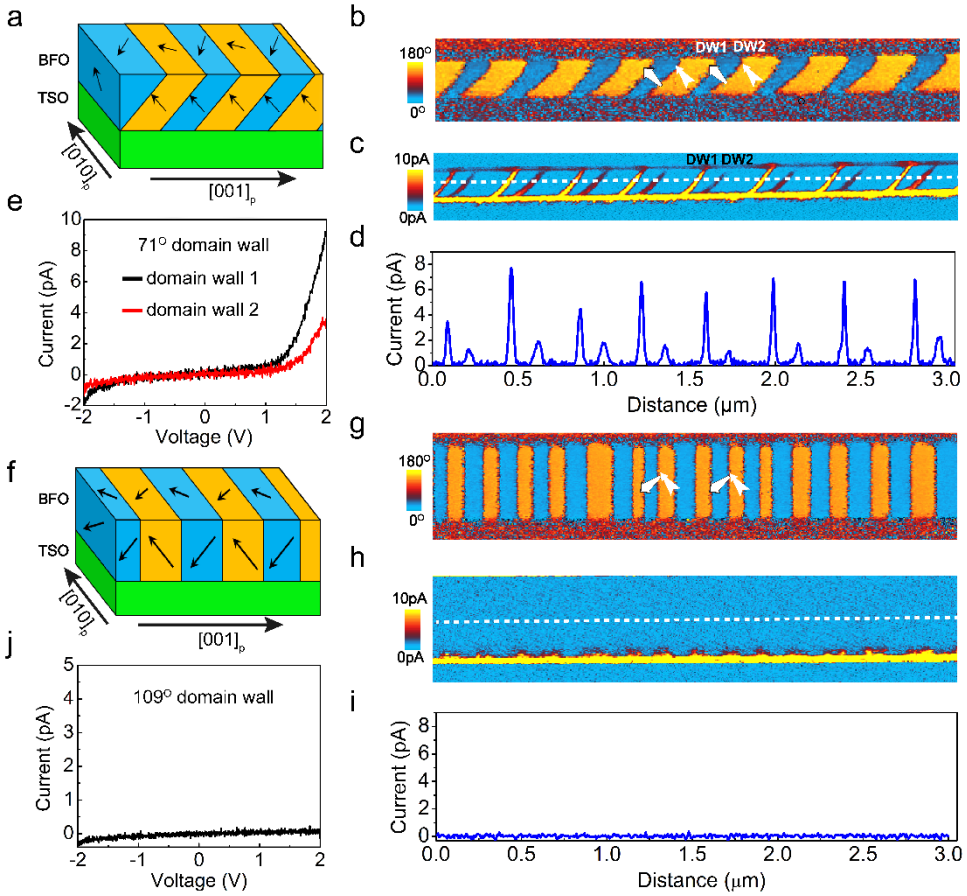

Figure 1 | Conductance for the 71° and 109°domain wall on cross section specimens. (a) Schematic illustration of the 71° domain array. (b) PFM phase image of cross-section BFO film with the 71° domain structure. The white arrows indicate the 3-dimensional polarization vector. (c) CAFM image of the same region as in (b). (d) The current profile along the white dotted line shown in (c). (e) The *I-V* curves measured on 71° walls on the cross-section sample. (f) Schematic illustration of 109° domain array. (g) PFM phase image of cross-section BFO film with the 109° domain structure. (h) CAFM image of the same region as in (g). (i) The current profile along the white dotted line in (h). (j) A typical *I-V* curve measured on the 109° wall on the cross-section sample. The sample thicknesses in $[010]_p$ direction in (a) and (f) are similar, which is around 1μm.

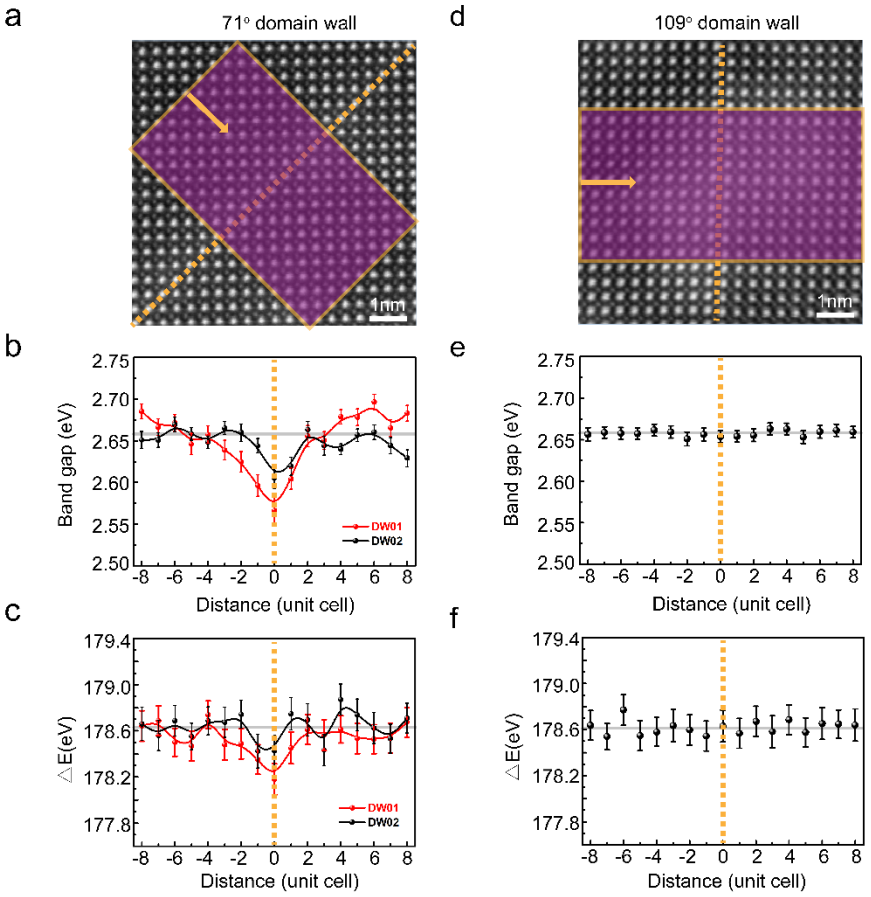

Figure 2 | Band gap and chemical profile at the 71° and 109° domain walls. (**a**) HAADF-STEM image obtained at the region of 71° domain wall. Orange dashed line indicates the 71° domain wall. High-resolution EELS line-scan were taken within the purple area in (a) and (d) along the directions indicated by the orange arrows, i.e. normal to the domain walls for both low-loss (**b**) and core-loss (**c**) measurement. (**b**) A band gap of two adjacent 71º domain walls (DW01 and DW02). The calculation of band gap energy from low-loss EELS can be seen in the Methods. Supplementary Figure S3 indexes the location of DW01 and DW02. (**c**) The energy onset difference between O-*K* and Fe-L_3 edges (ΔE) across two adjacent 71º domain walls (DW01 and DW02). ΔE is related to Fe oxidation state. (**d**) HAADF-STEM image obtained at 109° domain wall. Orange dashed line indicates the 109° domain wall. High-resolution EELS line-scan was taken within the purple area along the scan direction of the orange arrow, which is vertical to the domain wall direction, for both low-loss (**e**) and core-loss (**f**)

measurement. (**e**) Band gap of BFO across 109º domain wall. (**f**) The energy onset difference between O-*K* and Fe-L_3 edges across the 109º domain wall. In (**c**,**d**,**e**,**f**), the vertical orange dahsed lines indicate the location of corresponding domain walls. The gray dashed lines in (**b**) and (**e**) are located at 2.658 eV, which is average band gap from BFO bulk. The gray dashed lines in (**c**) and (**f**) are located at 178.63eV, which is average ΔE from BFO bulk**.**

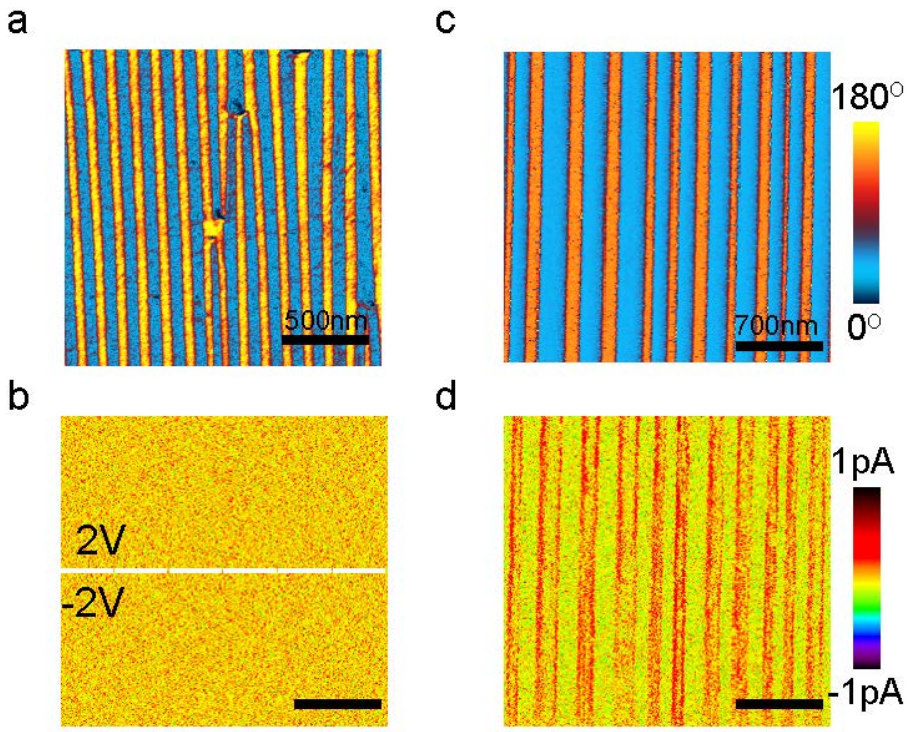

Figure 3 | Conductance for the 71° and 109° domain walls measured from film surface in BFO/TSO stucture. The thicknesses of the films with 71° and 109° domain are 200 nm and 400 nm, respectively. (**a**) Lateral PFM phase image showing 71° domain structure. (**b**) CAFM image of the same region as in (**a**). (**c**) Vertical PFM phase image showing 109° domain structure. (**d**) CAFM image of the same region as in (**c**).

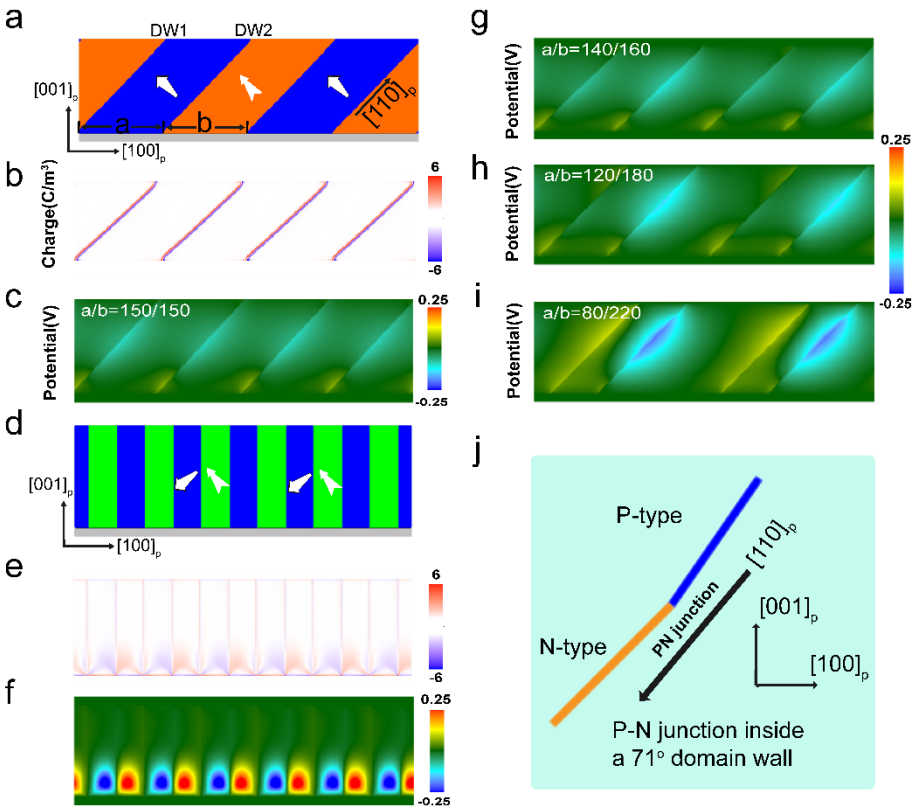

Figure 4 | Phase field simulations of the bound charge and potential distribution along the walls. (a) the 71° domain arrays used for phase-field simulations. The width of the two neighboring domains is defined as ***a*** and ***b***, respectively. The white arrows indicate the 3-dimensional polarization vector. (b,c) The bound charge distribution (b) and the corresponding potential distribution (c) around 71° domain walls separating domains of equal width. (d) The 109° domain arrays used for phase field simulations. (e,f) The bound charge distribution (e) and the corresponding potential distribution (f) around 109° domain walls. (g-i) Potential distribution around 71° domain walls separating domains of different width with ***a/b*** ratios of 140/160 (g), 120/180 (h), and 80/220 (i). (j) Schematic illustration of the p-n junction formed within a single 71° domain wall due to the wall bending.

Supplementary materials

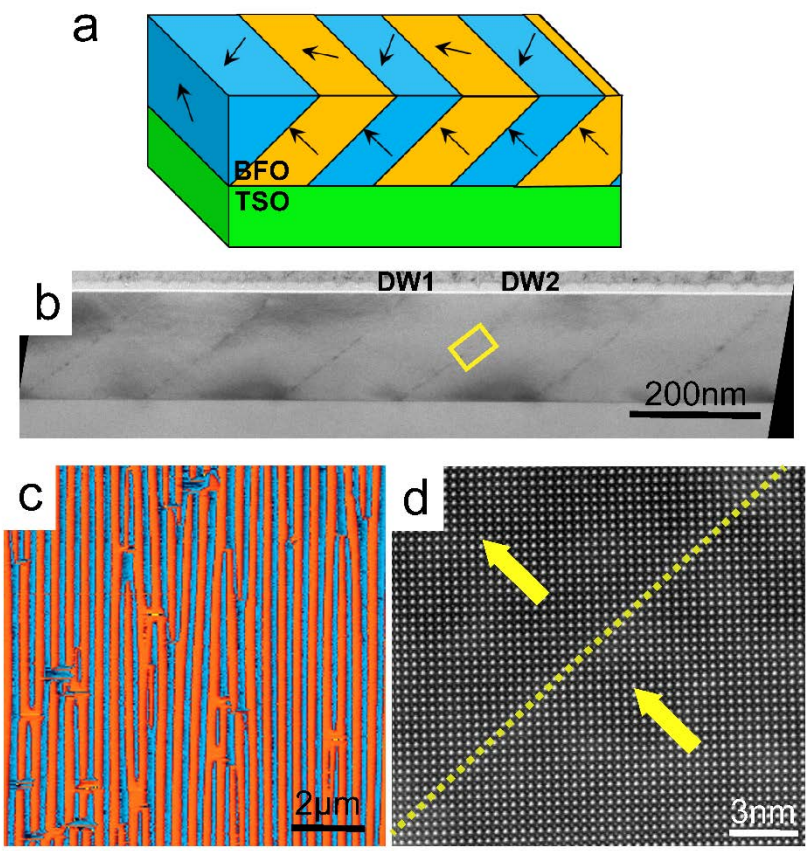

Supplementary Figure 1 | **71° domain array in the BFO film.** (a) Schematic illustration of the 71°domain array. (**b**) Low-magnification TEM image of the BFO/TSO cross-section. (**c**) PFM phase image of the BFO film with the 71° domain array acquired on the film surface. (**d**) High-resolution HAADF STEM image of the 71°domain wall in the area marked by the yellow rectangle in (b). Yellow arrows indicate the in-plane polarization directions, and a dashed line indicates the position of the 71° domain wall.

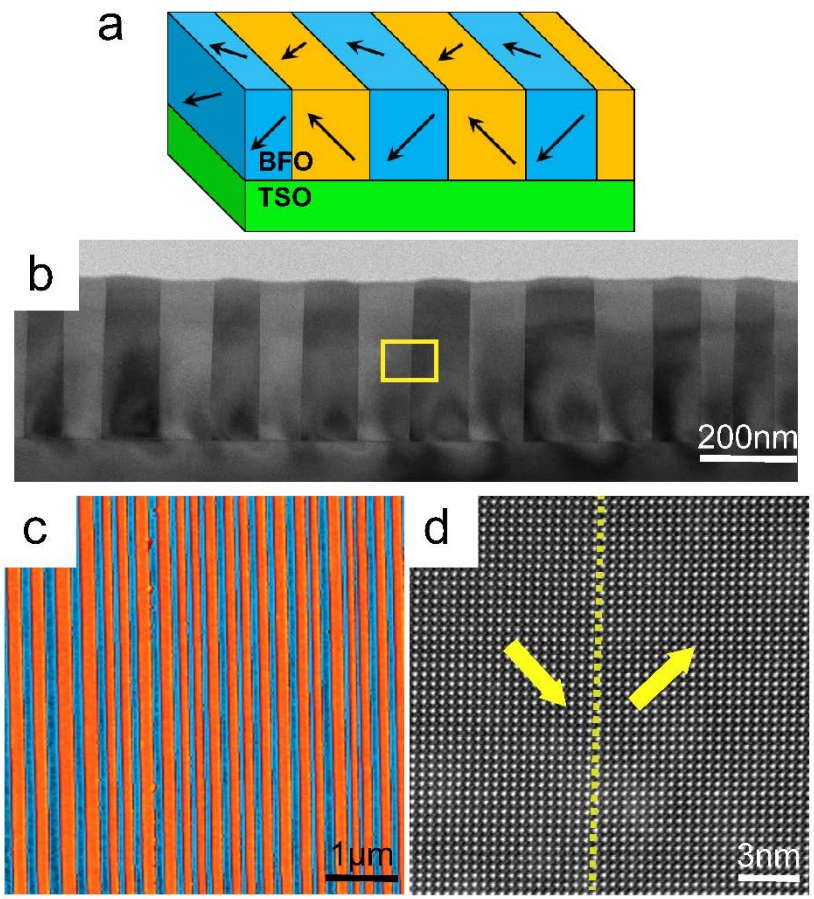

Supplementary Figure 2 | **109° domain array in the BFO film.** (**a**) Schematic illustration of the 109°domain array. (**b**) Low-magnification TEM image of the BFO/TSO cross-section. (**c**) PFM phase image of the BFO film with the 109° domain array acquired on the film surface. (**d**) High-resolution HAADF STEM image of the 109°domain wall in the area marked by the yellow rectangle in (b). Yellow arrows indicate in-plane polarization directions, and a dashed line indicates the position of the 109° domain wall.

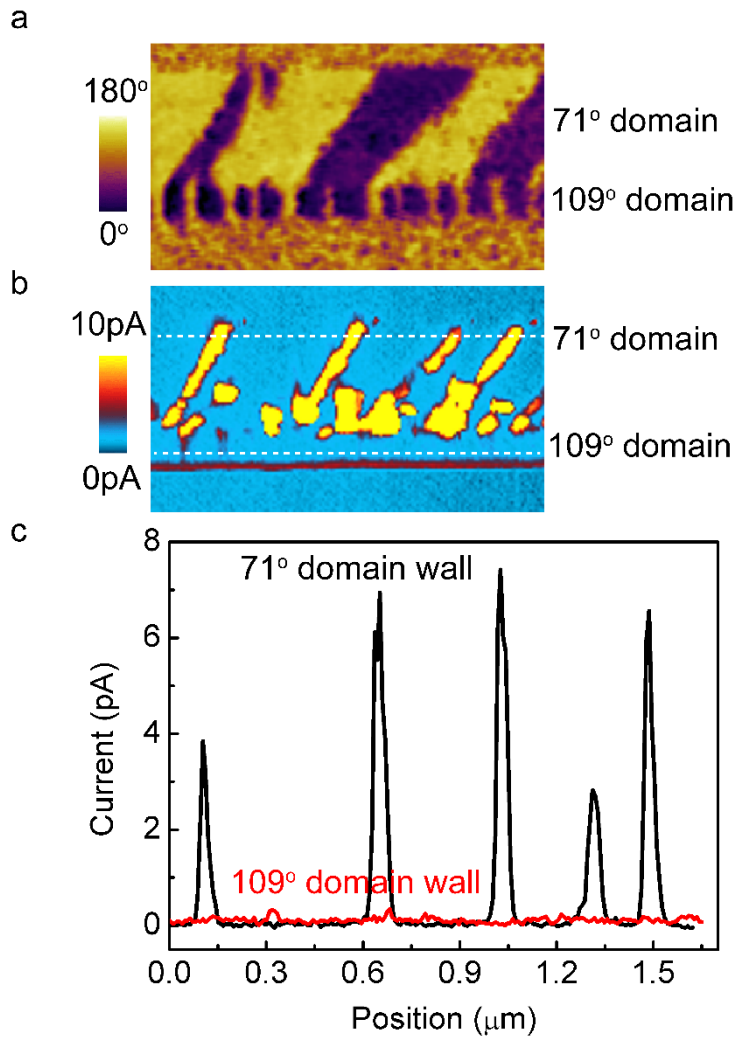

Supplementary Figure 3 | **CAFM measurements of domain wall conductivity in the cross-section samples with the mixture of 71° and 109° domains. (a)** PFM image of the domain structure composed of 71° and 109° domains. **(b)** CAFM image on the same region as in (a). **(c)** Current profiles for the 109° and 71° domain walls acquired along the white dash lines. The averaged current at the 71° domain walls is about 5 pA, while it is at the noise level of the equipment (0.5 pA) at the 109° domain walls. Therefore, we can estimate that the conductivity of the 71° domain walls is at least one order of magnitude larger than that of the 109° domain walls.

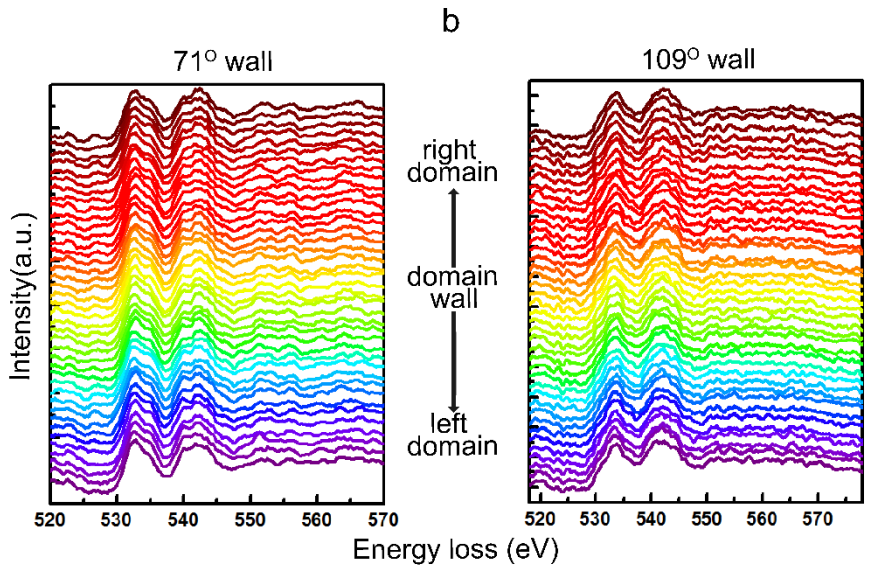

Supplementary Figure 4 | **Unchanged oxygen chemical environment at the domain walls.** Line-scan EELS core-loss EEL spectra of oxygen K-edge across domains in (**a**) 71° domain wall (DW01, from the same region shown in Figure 3a in the main text), and (**b**) 109° domain wall (the same region shown in Figure 3b in the main text). The corresponding location of each curve, including domain regions and domain wall, are indicated at the side of each figures. The onset and shape of oxygen curves are kept intact across both 109° and 71° domain walls, demonstrating that the local oxygen chemical environment doesn't change at the domain walls. Therefore, the domain walls in both samples with 109° and 71° domain arrays do not exhibit any impurity doping or strain effects.

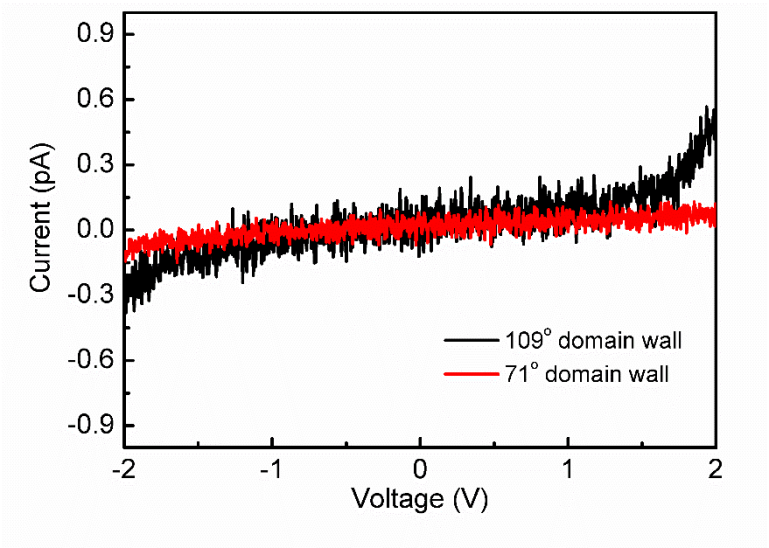

Supplementary Figure 5 | **Comparison of domain wall conductivity.** *I-V* curves measured at the 109° and 71° domain walls on the BFO film surface.

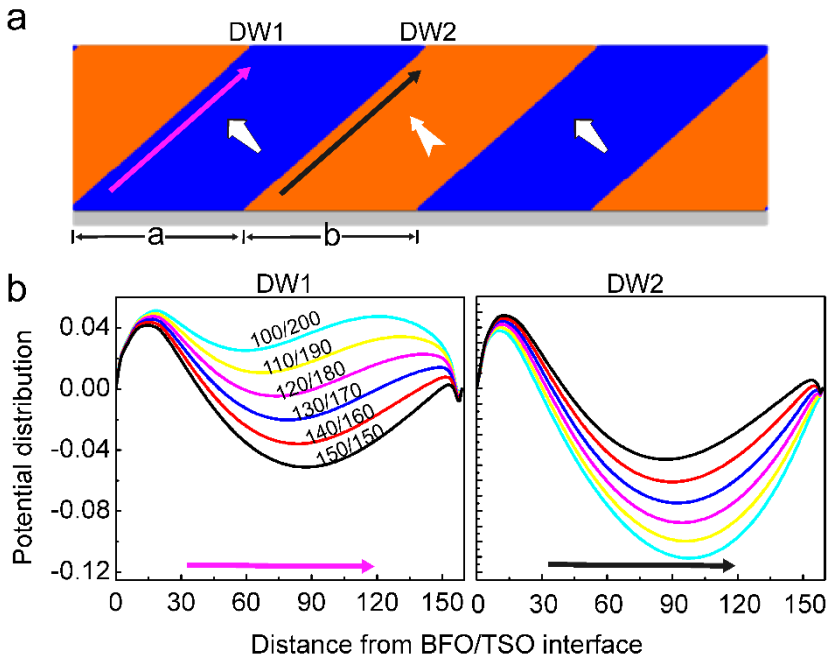

Supplementary Figure 6 | **Potential distribution along the 71º domain wall.** (a) The schematics of 71° domain arrays. The white arrows indicate the 3-dimensional polarization vector. (b) The potential profiles along the 71º domain walls directions (marked by the arrows in (a)) for domains with different ***a/b*** ratio.

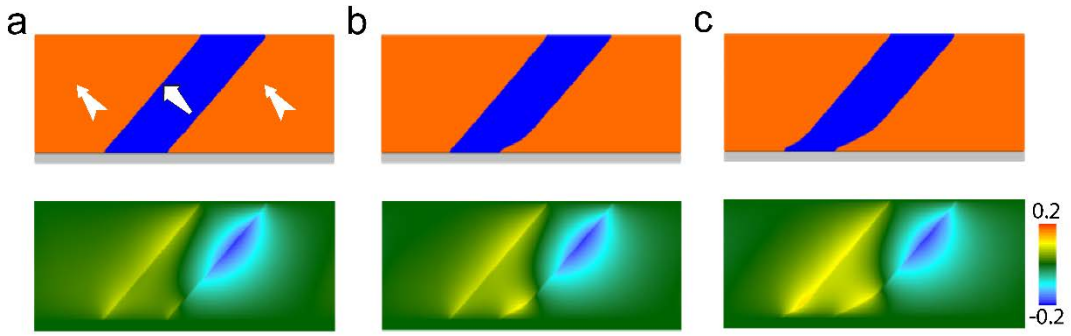

Supplementary Figure 7 | **Phase-field simulation of the 71º domain wall curvature effect on potential distribution.** (**a**) The pristin state of the 71° domain array (top panel) and the corresponding potential distribution (bottom panel). The white arrows indicate the 3-dimensional polarization vector. (**b** and **c**) Local curving of the domain wall (top panels) induces a positive potential inside the wall which is proportional to the curvature angle.